Symmetric rearrangement of groundwater-fed streams

Robert Yi[1], Yossi Cohen[1], Olivier Devauchelle[1], Goodwin Gibbins[1], Hansjörg Seybold[1], and Daniel H. Rothman[1]

[1] *Lorenz Center, Department of Earth, Atmospheric, and Planetary Sciences, Massachusetts Institute of Technology, Cambridge, MA*

July 31, 2017

Abstract

Streams shape landscapes through headward growth and lateral migration. When these streams are primarily fed by groundwater, recent work suggests that their tips advance to maximize the symmetry of the local Laplacian field associated with groundwater flow. We explore the extent to which such forcing is responsible for the lateral migration of streams by studying two features of groundwater-fed streams in Bristol, Florida: their confluence angle and their curvature. First, we find an anomalously wide 120° confluence angle within $\sim$ 10 m of the stream junctions and show that this wide angle maximizes the symmetry of the groundwater field near the junction. Second, we argue that streams migrate laterally within valleys and present a new spectral analysis method to relate planform curvature to the surrounding groundwater field. Our results suggest that streams can migrate laterally in response to fluxes from the surrounding groundwater table, providing evidence of a new mechanism that complements Laplacian growth at tips.

1 Introduction

River networks form captivating geometries, but their present-day position often obscures the rich history of their growth and evolution (Ritter et al., 2011). Fortunately, the processes that shape this history, such as the migration of river bends (Hickin and Nanson, 1984;

Bierman and Montgomery, 2013), stream capture (Howard, 1971b; Willett et al., 2014), and confluence movement and development (Carey et al., 2006; Unde and Dhakal, 2009), often leave behind morphological evidence. However, such processes have not been well-studied for groundwater-fed streams. In such landscapes, reemerging groundwater erodes surface grains by sapping and undermining hillslopes (Dunne, 1990; Howard and McLane, 1988), forming shallow streams and steep ravines around them. These streams advance in a planimetric direction that has been shown to be largely determined by the shape of the surrounding groundwater field rather than dynamics within the stream (Devauchelle et al., 2012; Petroff et al., 2013). In particular, recent work suggests that this advance maximizes the symmetry of the local groundwater field (Cohen et al., 2015; Devauchelle et al., 2017). For a confluence, this predicts an angle of $2\pi/5 = 72^\circ$ between confluent streams, and these observations have been observed in the planimetry of a groundwater-fed channel network in Bristol, Florida (Devauchelle et al., 2012).

However, there is no indication that the current position of channels within valleys in such networks represents the history of their growth. We therefore consider a third phase of growth: lateral stream rearrangement. We suggest that this rearrangement is also influenced by the surrounding groundwater field. In particular, we hypothesize that lateral migration is driven by variable flux to either side of a stream and the subsequent filling-in of old stream paths through soil creep. Here we study two morphological features of a groundwater-fed river network to constrain the extent to which this groundwater field can describe network-wide morphology: confluences and planform curvature.

This rearrangement may be of wider interest, both observationally and theoretically. First, recent work has demonstrated that an average branching angle of 72° appears in humid climates (Seybold et al., 2017), suggesting that the influence of groundwater on river planform morphology may be widespread wherever shallow groundwater is present. Second, as we will shortly explain, the height squared of the groundwater table solves Poisson's equation and, close to the streams, Laplace's equation. Because these streams can be approximated as

effectively one-dimensional, their advance can be understood as an example of thin-finger Laplacian growth (Gubiec and Szymczak, 2008; Carleson and Makarov, 2002; Cohen et al., 2015). Our results therefore present a novel mechanism for and example of lateral migration of a thin-finger boundary in response to a Laplacian field.

In what follows, we present evidence of this rearrangement from a network of streams in Bristol, Florida and discuss how it may arise. We first review a theoretical framework that gives the shape of the groundwater table and the 72° branching angle. We also present an averaging scheme that reveals a striking 120° angle near the junctions of first-order confluences in Bristol, Florida. We then present a model for the migration in response to asymmetry in the groundwater field that predicts the observed deviation. Next, we show how the spectral analysis of streams can differentiate between clockwise and counter-clockwise downstream flow, and we use this method to find a length scale of curvature fluctuation that agrees with the length scale of the confluence deviation. Finally, we find evidence for network-wide river migration, suggesting that forcing from groundwater may influence stream planimetry throughout the network.

2 Background

2.1 Groundwater flow

Groundwater-fed channels advance as reemerging groundwater erodes material, causing the intersection point between the groundwater table and the ground to retreat, thereby extending the channel (Dunne, 1990). We begin by reviewing a theoretical framework that can describe these dynamics. Consider a lone channel advancing in a groundwater field. Pressure gradients from the surrounding groundwater table determine where and how the groundwater flows into this channel (Darcy, 1856; Polubarinova-Kochina, 1962). When these gradients are hydrostatic and flows are approximately horizontal, groundwater flux q (per unit length in the horizontal plane) can be be simply described through Darcy's law in the

Dupuit approximation (Darcy, 1856; Dupuit, 1863; Bear, 1972):

$$q = -kh\nabla h, \tag{1}$$

where k is hydraulic conductivity and h is the height of the groundwater table. Mass conservation between flux out of the groundwater table and precipitation into it yields Poisson's equation for h^2 (Bear, 1972):

$$\nabla^2 h^2 = -\frac{2P}{k}, \tag{2}$$

where P is the precipitation rate. Sufficiently close to a stream, precipitation P can be neglected, yielding Laplace's equation (Devauchelle et al., 2012; Petroff et al., 2013):

$$\nabla^2 h^2 = 0 \tag{3}$$

This equation can be solved around a real channel network, and this solution has been shown to accurately predict the shape of the water table (Abrams et al., 2009) and flow into the channel network (Petroff et al., 2011).

2.2 Growth direction

The solution to (3) can be combined with a growth hypothesis to predict how the channels grow forward. Recent results (Cohen et al., 2015; Devauchelle et al., 2017) suggest that streams grow in a direction that can be equivalently described by three growth hypotheses: streams maintain symmetry of the groundwater table around the spring as they grow, streams grow in the direction of the streamline entering the spring, and streams grow in the direction of maximum flux entering the tip. When a channel develops a confluence upstream, the streamlines enter the springs without curving when the angle between the confluent streams is 72° (Devauchelle et al., 2012; Petroff et al., 2013). If streams advance at an angle narrower than 72°, the streamlines entering the two springs will bend away from each other; if streams

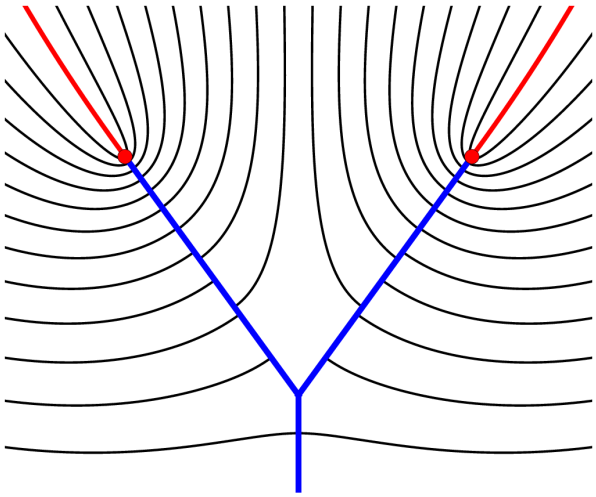

Figure 1: Streamlines around a confluence with an angle of $2\pi/5$ between confluent streams. The tip locations are marked as red dots. The streamlines entering the tips are indicated in red, while all other streamlines are black. The stream is blue.

advance at an angle wider than 72°, the streamlines entering the springs will bend toward each other (Devauchelle et al., 2012; Petroff et al., 2013). The 72° confluence therefore can be considered a stable fixed point for stream advance (Devauchelle et al., 2017). An illustration of such a confluence and its streamlines are shown in Figure 1.

This predicted shape agrees with the average angle at which confluent streams join in a river network in Bristol, Florida, determined by fitting individual streams to straight lines (Devauchelle et al., 2012). However, as we will demonstrate, real confluences deviate from this theory. We now proceed to briefly describe the field site used and methods employed to this end.

3 Confluence migration

3.1 Wide angle confluences in Bristol, Florida

Confluences are ubiquitous in river networks, but the often sedimentologically complex dynamics that form them thwart attempts to construct a unifying theory for their development. River confluence geometry can be influenced by a number of parameters: relative flow mag-

Figure 2: A confluence in the Apalachicola river network in Bristol, Florida. The white lines indicate the location of the streams with arrows denoting the flow direction.

nitudes and the depth of the deepest point along a stream bed (thalweg incision) (Kennedy, 1984), the overall power exerted by the network (Howard, 1971a), fluid and sediment transport dynamics (Best, 1988), scour depth (Mosley, 1976), among others. However, these factors may not be the primary factors influencing migration in landscapes formed primarily through erosion by groundwater reemergence.

We study streams from a network of groundwater-fed streams located on the Florida panhandle. These rivers are overlain by homogeneous sediment comprised primarily of unconsolidated quartz sand (Abrams et al., 2009) which rests atop a layer of impermeable clay (Schumm et al., 1995). The high hydraulic conductivity $k \sim 10^{-4}$ m s^{-1} of such clean, unconsolidated sand causes rainfall $P \sim 5 \times 10^{-8}$ m s^{-1} to be quickly absorbed, prohibiting surface runoff (Abrams et al., 2009). This supports a persistent water table in the subsurface. We first consider only first-order streams (those without any upstream confluences). These streams are shallow, with little evidence of scouring or deposition, negligible difference in bed height (bed discordance), minimal difference in discharge, and negligible suspended load (Schumm et al., 1995); these properties make this field site ideal to study the influence of groundwater seepage in isolation from factors that typically influence confluence geometry. An example of such a confluence is shown in figure 2. These streams are roughly $\sim$ 20 cm

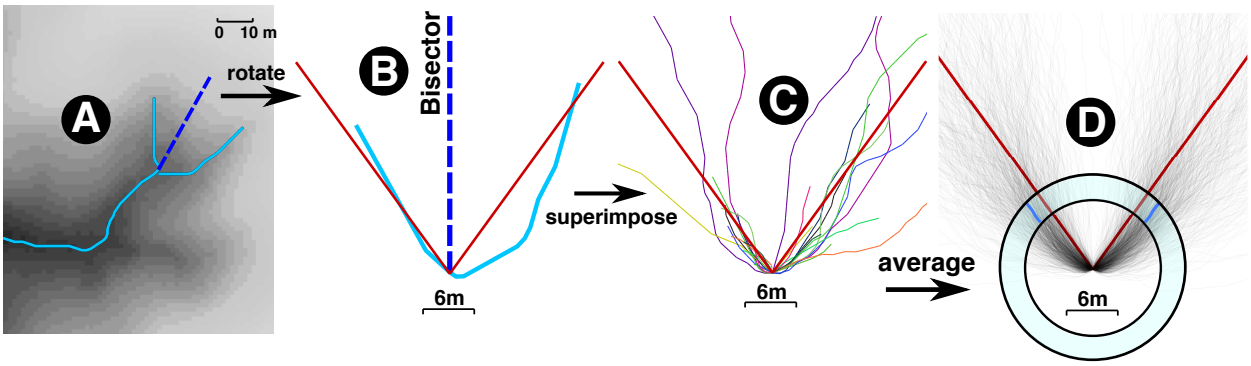

Figure 3: An illustration of our confluence averaging method. (a) A first-order confluence, (b) rotated along its bisector, with (c) a few of these streams superimposed. (d) All 1225 first-order confluences shown in grey, set against 72° lines in red. We illustrate the averaging scheme in the annulus: we take radial slices from confluence junctions and average the polar angle for each stream within these slices.

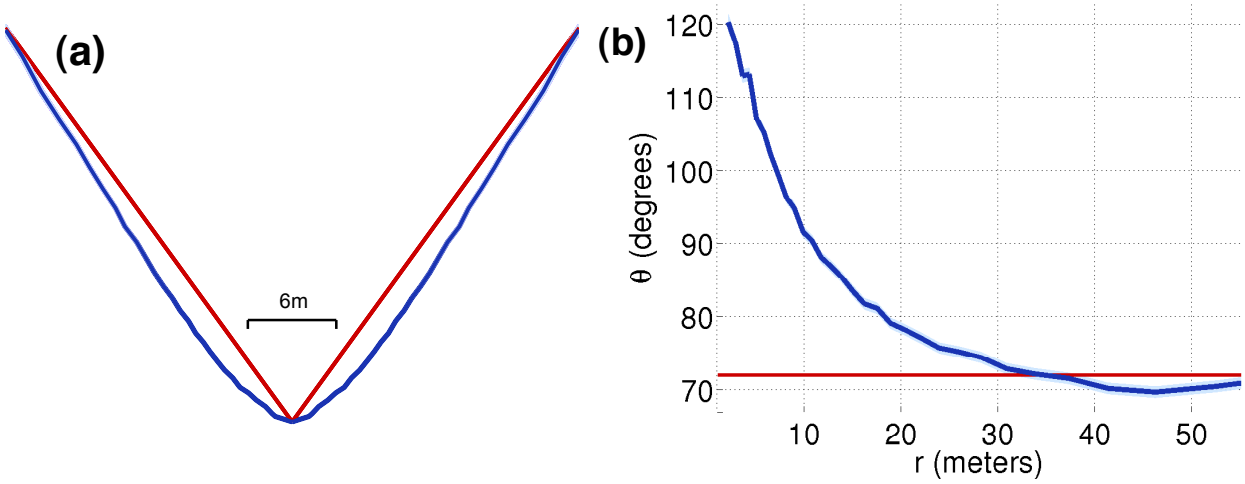

Figure 4: (a) Average shape of 1225 confluences in our network, shown in blue against a 72° confluence (red). The light blue shaded region around these lines (hidden mostly by the line) indicates the standard error of the mean. Each point along the trajectory here represents the average of 1300 observations. A small resolution anomaly occurs in these averaging schemes close to the junction due to the limit of our grid resolution (1.2 m) and should be neglected. (b) The same data from (a) transformed to polar coordinates to demonstrate the behavior of the polar coordinate θ as measured from the junction. The previously mentioned resolution anomaly over the first 1.2 meters is omitted.

in width and ~ 1 cm in depth (Devauchelle et al., 2010).

We extracted the location of streams in Florida by thresholding the curvature of topographic contours, obtained from laser altimetry data with a horizontal resolution of 1.2 m and a vertical resolution of about 5 cm (Devauchelle et al., 2012), as outlined by Devauchelle

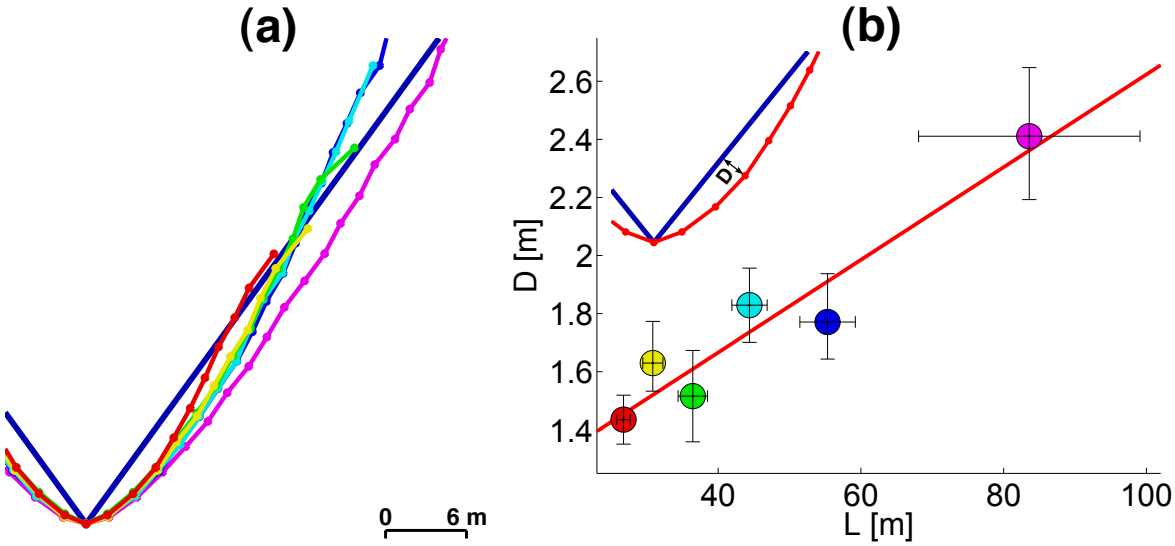

Figure 5: (a) Spatially averaged curves (binned by the same mechanism as in figure 3). Each point represents the average of 250 points. (b) The maximum distance D from the 72° lines against the average length L of these streams. The error bars in L indicate the standard deviation and the error bars in D indicate standard error of the mean. The inset on the top left illustrates the measurement D.

et al. (2010). We ordered our channels according to Horton-Strahler ordering (Horton, 1945; Strahler, 1952) and aligned first-order confluence pairs along their bisector, as determined by the sum of the vectors obtained from regression of each of the two confluent streams. To obtain angle as a function of distance from the junction, the aligned channel coordinates were converted to polar coordinates, and angle was averaged for each stream as a function of distance from the junction, as illustrated in Figure 3.

A network-wide averaging of 1225 confluences from our field site by this method is shown in figure 4(a), where each point represents an average of points within a radial slice. Figure 4(b) quantifies the angle as a function of distance from the junction by transformation of the shape in figure 4(a) to polar coordinates. We note that the shape exhibits a wide angle deviation ($\sim 120°$) from the predicted 72° angle near the junction. We note that this averaging scheme is not necessarily representative of the archetypal groundwater-fed stream confluence shape, but a visualization of where channels are located on average.

There are three symmetric geometric adjustments that may give rise to this wide angle

deviation: (1) headward growth in a direction that follows the deviant trajectory, (2) movement (advance) of the junction, or (3) lateral migration of the channel after growth. We hypothesize that the lateral migration of channels is responsible for the deviation from 72° we observed in figure 4. The average channel location therefore represents a balance between migrational forcing and confinement by valley sidewalls. We therefore assume that figure 4 represents a statistical steady-state configuration.

To investigate these assumptions, we repeat the averaging scheme of Figure 4 for channels sorted by arclength between spring and junction, precluding particularly small (< 25 m) and large (> 120 m) channels from this analysis. Channels averaged in this manner are shown in Figure 5, where different average channel lengths correspond to different colors. As channel length increases, the size of the deviation from the 72° lines increases (figure 5(b)), which suggests that the strength of confinement within valleys decreases with channel length. This is consistent with confinement caused by diffusion of the valley sidewalls, which are steepest near the springs. This observation will be discussed further when we talk about the characteristic scales associated with network-wide fluctuations in curvature.

3.2 A mechanism for lateral migration

We hypothesize that forcing from an asymmetric groundwater field downstream is responsible for this lateral stream migration, as streams adjust to the flux difference from their two sides. While self-similar branches with a 72° angle between them have a locally symmetric field around their tips, this field is not symmetric downstream from the tips. An illustration of this asymmetry is shown in figure 6(a). Consider again the confluence geometry in which the two confluent streams are finite and mirror symmetric about a third, semi-infinite stream downstream. Let α be the angle between these two finite branches. Denote the region between them as the "inside" and the regions between each branch and the semi-infinite branch as "outside," as labelled in Figure 6(a). We reference these two regions with the subscripts i and o, respectively. The flux from the inside is therefore $Q_i(s)$ and, from the

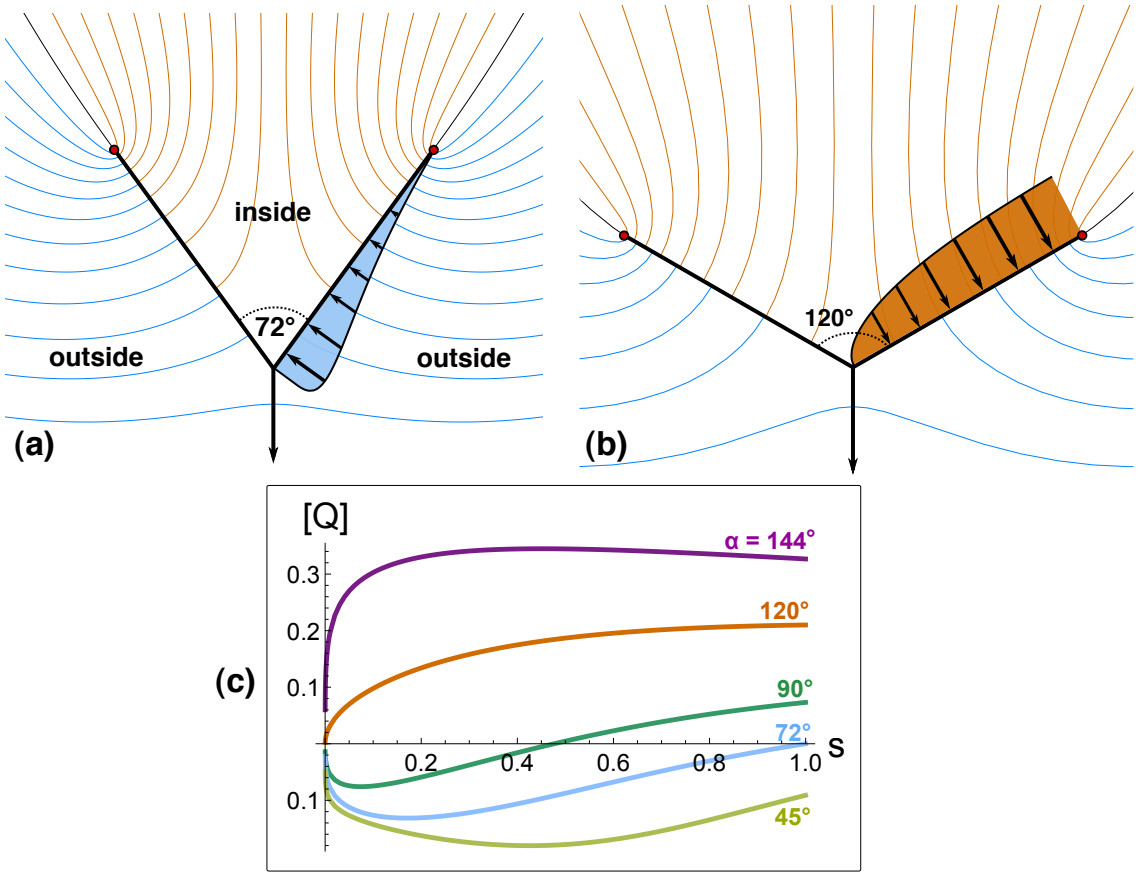

Figure 6: (a) Illustration of the flux asymmetry into stream confluences branching at an angle of 72°. The parent channels (oriented vertically) extend infinitely. The density of streamlines indicates the flux density. The uneven streamline spacing downstream of the tips suggests that the field is asymmetric. The shaded region is the difference between the fluxes into these two sides, indicating that the flux is larger on the shaded side. The orange and blue colors indicate association with the inside of the angle and the outside, respectively. (b) The same illustration as (a) but with a confluence angle of 120°. (c) Flux jump $[Q]$ as a function of arclength measured from the junction s (rescaled by length of the branch) for Y-shaped confluences of varying confluence angle α.

outside, $Q_o(s)$, where s is the arclength measured from the junction. We define the *flux jump* $[Q(s)]$ as

$$[Q(s)] = Q_i(s) - Q_o(s). \tag{4}$$

Symmetry arguments provide some intuition about the geometry that migration according to $[Q(s)]$ would produce. When $\alpha = 72°$, the field is locally symmetric at the tips (Cohen et al., 2015) and so $[Q(s)] = 0$ at the tips. Therefore, no lateral migration would occur at

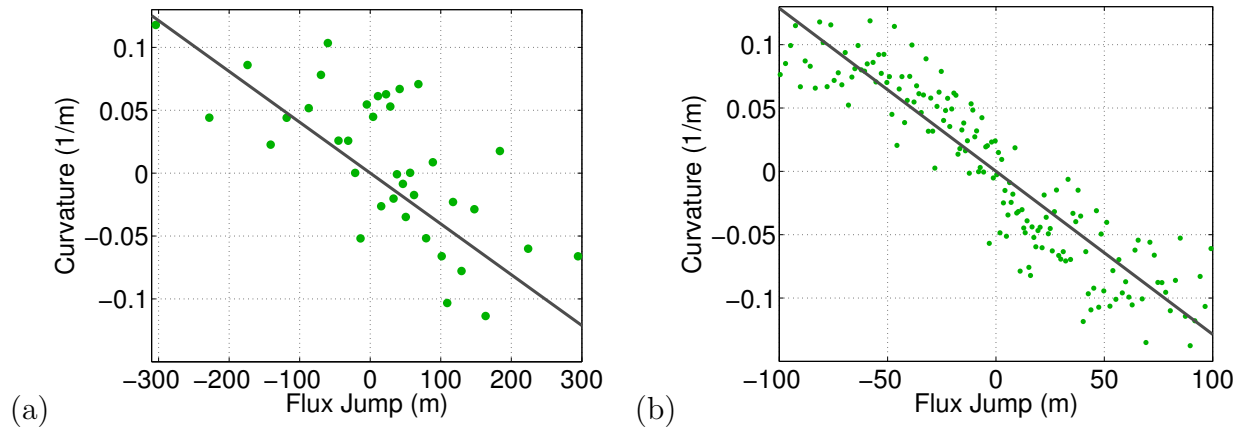

Figure 7: (a) Curvature against numerically calculated flux jump for first-order confluences. The dark grey line is a fit of slope -4×10^{-4}, implying $\lambda \approx 47 \pm 18$ m. Each green point represents the average of 10 observations. (b) Curvature against flux jump for all channels in the network. The dark grey line corresponds to a slope of -0.0013 or a value of $\lambda \approx 27 \pm 1$ m. Each point represents the average of 100 observations.

the tips. Close to the junction, the two confluent streams appear infinitely long, becoming locally indistinguishable from the second-order, infinitely long downstream channel. When $\alpha = 120°$ and all three branches are infinitely long, the field will be symmetric on either side of each channel, producing flux jump $[Q] = 0$ everywhere. When the confluent streams are finite, $[Q(s)]$ increases most slowly with s when $\alpha = 120°$ (see Appendix A for proof). Consequently, the flux jump near the junction is minimized when $\alpha = 120°$, and the angle $\alpha = 120°$ can be understood as the most stable angle near the junction. We therefore hypothesize that real channels that migrate according to this flux jump exhibit a $\sim 120°$ angle near the junction and a $\sim 72°$ angle near the tips. These predictions agree with the angles of real confluences near the junction and tips, respectively, shown in Figure 4(f).

The flux-dependent migration process we have discussed thus far suggests that streams migrate with velocity v_m perpendicular to themselves at a rate which grows with the flux jump. Assuming a linear response, we then have

$$v_m(s) = \epsilon[\hat{Q}(s)] - \nu\kappa(s), \tag{5}$$

where

$$[\hat{Q}(s)] = Q_l - Q_r. \tag{6}$$

$[\hat{Q}(s)]$ is the flux jump across the river at an arclength s with units of m. Q_l is the flux from the left of the stream when facing downstream and Q_r is the flux from the right. We use left and right here rather than inside and outside so that $[\hat{Q}(s)]$ behaves consistently with the sign of curvature. This flux is the Poisson flux, which represents the area drained per unit arclength (Petroff et al., 2011). Explicitly it is flux in m^2/s divided by precipitation rate. The quantity v_m is the perpendicular velocity at which the channel is migrating, ϵ is a constant with units s^{-1}, ν is a constant with units m^2/s, and κ is the local signed curvature (Weisstein, 2017). A negative curvature indicates that, when facing downstream, a channel rotates counter-clockwise. The $\nu\kappa$ term represents a stabilizing effect that can be understood as a first-order approximation to the influence of soil creep as streams migrate against the valley wall.

If this stabilization is balanced by the flux difference across the stream and the streams are in a statistical steady state, we have

$$v_m = 0 \tag{7}$$

and therefore,

$$\lambda^2 \equiv \frac{[\hat{Q}(s)]}{\kappa(s)} = \frac{\nu}{\epsilon}. \tag{8}$$

Physically, λ^2 represents the difference in area drained on either side over the length of the curve. The ratio of $[\hat{Q}]$ to κ therefore provides a ratio ν/ϵ with units of m^2. We note that this steady-state assumption requires only that ν and ϵ be of the same sign. However, we expect that the sign of ϵ is positive, representing a migration towards the side of the stream that draws greater flux. We will provide evidence of this in section 4.2.

We calculate $[\hat{Q}]$ and κ for a number of first-order confluences in our network, shown in Figure 7(a) and for all channels in our network, shown in figure 7(b). We restrict these

measures to a portion of the network for which we have LIDAR data that can clearly resolve curves in these streams. The slope of these lines can be used to obtain λ, which scales with the characteristic difference in distance to the drainage divide on either side of a stream, over the length of a curve in that stream. For all streams in our network on average, $\lambda \sim 30$ m. Since the characteristic distance to the drainage divide is ~ 100 m (Petroff et al., 2013), this suggests that the field asymmetry produces a deviation in stream shape whose size corresponds to roughly 15% of the characteristic distance to the divide. We will now briefly explore the shapes of network-wide curves to explore precisely how this steady state shape appears on the network scale.

4 Network migration

4.1 Network-wide power spectrum

To study how these stream curves appear in the network-wide regime, we measure the periodicity of network-wide fluctuations in curvature. A representative channel colored by curvature is shown in figure 8.

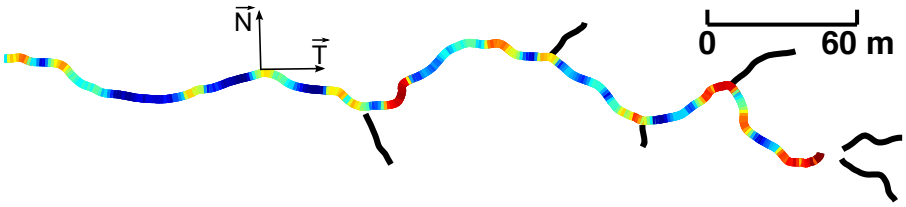

Figure 8: A second-order channel colored by curvature.

Determining the periodicity of stream curvature requires a rotation-invariant, differential representation of the geometry. Traditionally, these periodicities are studied through spectral analysis of the angle or curvature (Ferguson, 1975; Marani et al., 2002). However, while these methods are sufficient in isolating the primary frequency of curvature fluctuation, they ignore phase information that might reveal asymmetries in the growth. We therefore offer an alternative method: we rewrite our signal in terms of the 2D Frenet equations. The

Frenet equations fully describe the relationship between tangent vectors, normal vectors, and curvature on a twice continuously differentiable curve (Kühnel, 2015):

$$\frac{d\vec{T}}{dt} = \kappa\vec{N}, \tag{9}$$

$$\frac{d\vec{N}}{dt} = -\kappa\vec{T}, \tag{10}$$

where $\vec{T}$ and $\vec{N}$ are the tangent and normal vectors to the curve. We calculate the tangent vector over 3 meters (as determined by the vector drawn between the two points surrounding the point in question) and curvature over 5 meters for each point in all first-order channels, to obtain the $d\vec{N}/dt$. No additional information in carried in $d\vec{T}/dt$, so we can use $d\vec{N}/dt$ without loss of generality. We write the tangent vector $\vec{T}$ as a single imaginary number $T_x + iT_y$, where T_x and T_y are the x and y components of $\vec{T}$, and $i^2 = -1$. Equation (10) becomes

$$\frac{d\vec{N}}{dt} = -\kappa(T_x + iT_y). \tag{11}$$

The averaged power spectra of (11) for channels of all orders in our network is shown in figure 9. The power spectrum of (11) is roughly equivalent to the power spectrum of κ alone, but the sign of the frequency spectrum also indicates whether the channel is moving counterclockwise (positive) or clockwise (negative) as one travels downstream from the tip. The network-wide effect of this bias is reflected in the slight asymmetry of Figure 9(a). Positive and negative frequencies are combined in Figure 9(b) and in subsequent figures.

We now calculate the power spectra separately for first-, second-, and third-order channels and average them, shown in Figure 9(c). We only use streams longer than 50 meters for this calculation, to diminish the effect of the length distribution on the power spectra. Stream curvatures in our network appear to fluctuate at a dominant frequency that corresponds to a wavelength of 26.7 m for first-order channels, 28.3 m for second-order channels, and 28.4 for third-order channels. The higher power spectral density of the second and third-order channels results from higher values of curvature in second-order channels. However, because a

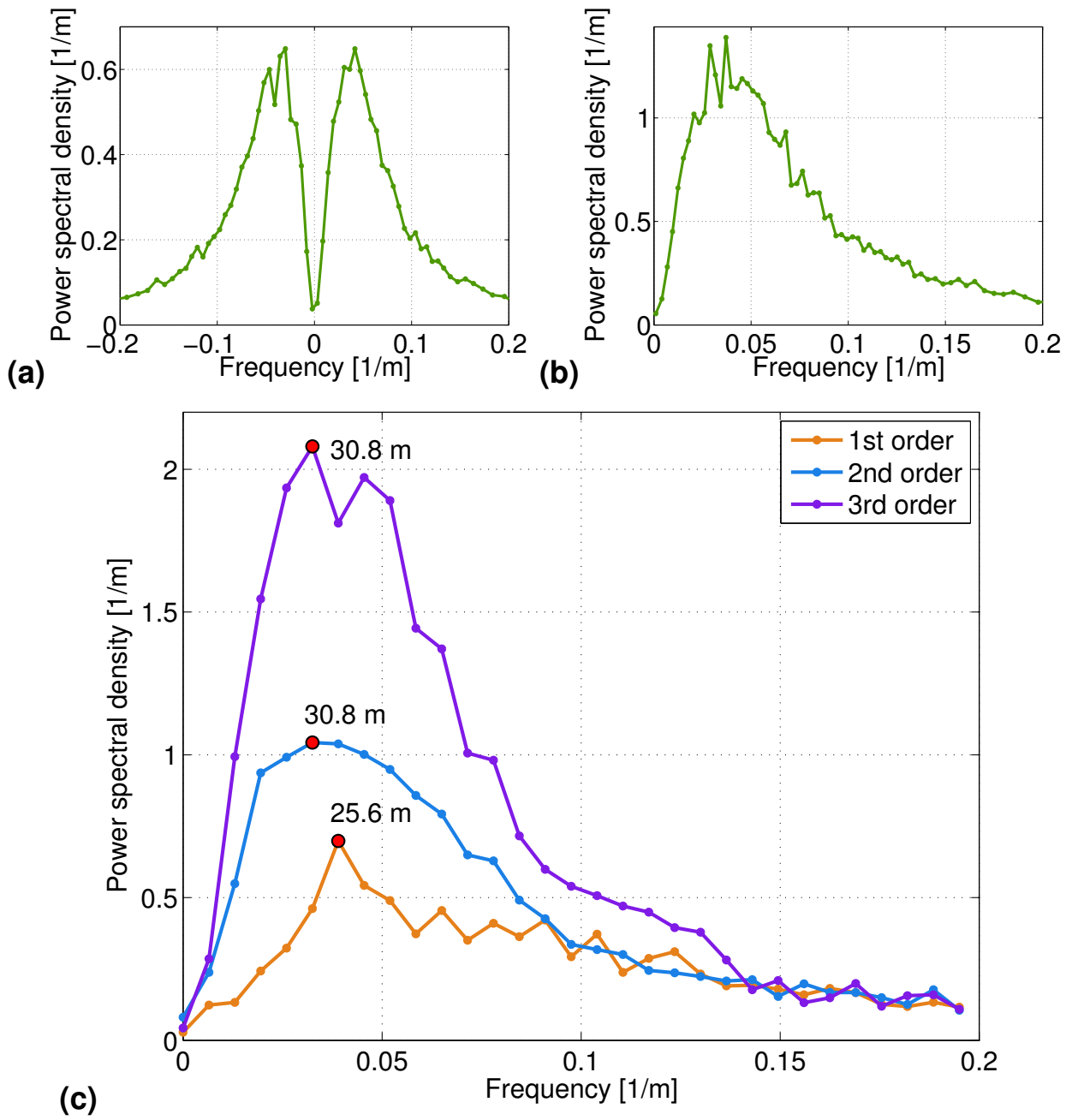

Figure 9: (a) The averaged power spectrum of channels (all orders) in the Bristol, Florida network, binned by frequency. The asymmetry reflects the direction in which channels turn: clockwise (negative frequencies) or counterclockwise (positive) from the tip. (b) The same data as (a), symmetrized. (c) The averaged power spectrum of $\frac{d\vec{N}}{dt}$ for first-order channels in orange, second-order channels in blue, and third-order channels in purple. The red dots indicate the peaks of these curves, labelled with the corresponding periodicity in meters.

higher value of curvature generates an increased wavelength by simply extending the channel arclength, the correspondence of first-order and second-order channel curvature wavelengths

may be even closer than we have found. The agreement of this ~ 30 m wavelength to the length scale over which the wide opening angle of confluences returns to the 72° lines (seen in the intersection between the light blue and red lines in Figure 4(f)) suggests that both network-wide fluctuations in curvature and confluence migration may be influenced by a common mechanism.

This spectral analysis resembles analyses conducted on river meanders, which form as flowing water erodes river banks and redeposits eroded sediment downstream (Speight, 1965; Hooke, 1984; Gutierrez et al., 2014). However, we contend that the distinct morphology of the streams we study here suggests that they were shaped by different processes than those typically attributed to the formation of river meanders. For meanders confined by valley walls, the meander wavelength is ~ 17 times larger than the width of the meandering river (Nicoll and Hickin, 2010). In contrast, first-order channel widths in the Bristol, Florida network range from $\sim 10-20$ cm near the springs up to 50 cm near downstream confluences, producing a ratio of wavelength to channel width of $\sim$ 50-500. Streams in our network also have a sinuosity (defined as the ratio of channel length to valley length) < 1.3, which would generally be classified as "straight", rather than "meandering" (Bierman and Montgomery, 2013). We therefore suggest that the fluctuations reflected in Figure 9 are not primarily the result of erosional dynamics typically associated with river meanders, though the increased curvature in higher order streams may signify an increasing importance of typical meandering dynamics downstream as confinement by valley sidewalls decreases. This behavior is consistent with our observation in figure 5 that the size of the deviation of confluences from 72° increases with channel length. Finally, the independence of curvature wavelength with order suggests that this length scale is initially set by factors independent of dynamics within the streams and only later augmented by such dynamics, if at all.

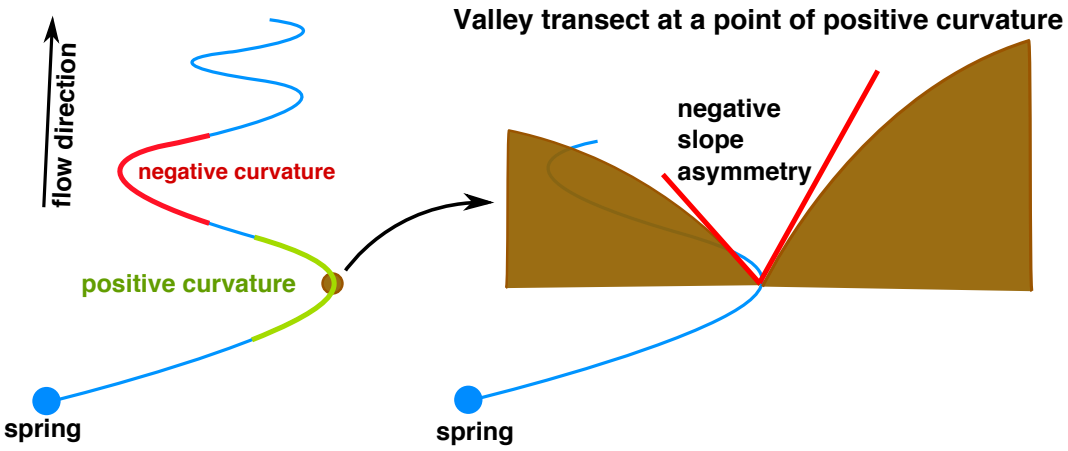

Figure 10: An illustration of the physical interpretation of the sign of curvature and slope asymmetry, as defined in the text.

4.2 Evidence of network-wide migration

We now present field evidence that these channels are indeed migrating in the manner we suggest. We measure slope asymmetries along the valley sidewalls, which we define as the valley sidewall slope on one side subtracted from the other. We hypothesize that, if channels are laterally migrating, they should steepen the sidewall which they migrate into.

We quantify the slope asymmetry by extracting the channel direction over a window of four meters along all channels in the network. We then obtain values of slope over 10 meters on either side of the channel along the axis perpendicular to this direction from LIDAR data. We take the steepest 20% of these slopes and average them, under the assumption that the steepest sections of a valley represent the steepest steady-state configuration sustainable by a balance between sediment transport and diffusive transport. Facing downstream, we call the averaged slope to the left of the stream S_l and to the right, S_r. We then calculate the slope asymmetry, which we define as $(S_l - S_r)/(S_l + S_r)$. This quantity is therefore positive when the steeper slope is on the left and negative when on the right.

We compare slope asymmetry, curvature, and flux jump as defined in equation (6). The signs of curvature and slope asymmetry are illustrated in Figure 10. The relationship between slope asymmetry and curvature is shown in figure 11(a). A negative curvature indicates a

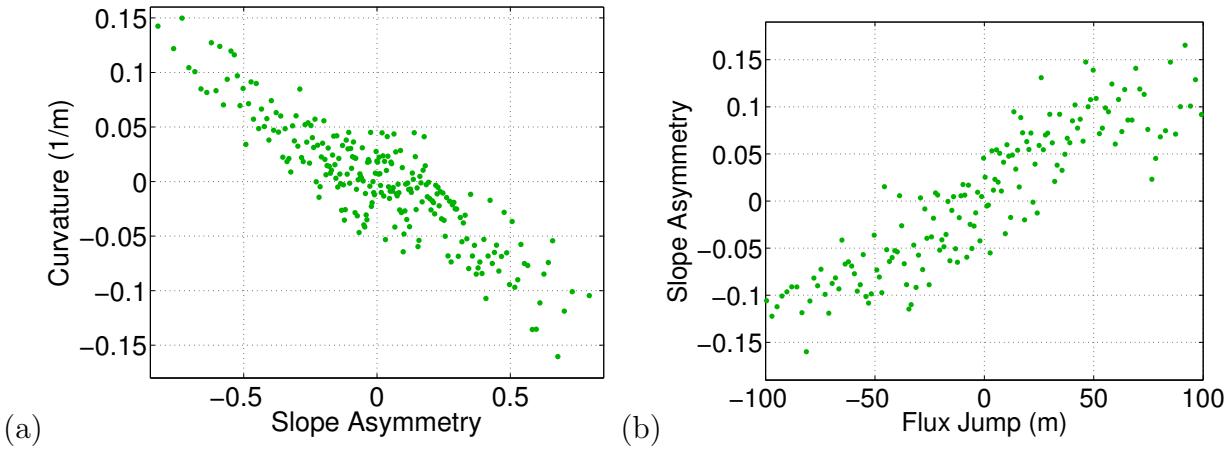

Figure 11: For both plots, each point is the average of 100 observations. (a) Curvature against slope asymmetry, as defined by $(S_l - S_r)/(S_l + S_r)$, where S_l and S_r are the slopes to the left and right of the stream, r spectively, when facing downstream. (b) Slope asymmetry against flux jump, $(Q_l - Q_r)$, where Q_l and Q_r are the fluxes from the left and the right of the stream, respectively, when facing dowstream.

negative second-derivative: facing downstream, this corresponds to a channel that rotates counter-clockwise. Negative values of curvature appear to correspond to positive values of slope asymmetry, suggesting that the valley side into which a channel veers has a higher slope. The data for flux jump against slope asymmetry, shown in figure 11(b), also scale linearly. This suggests that the steeper side of the valley tends to draw greater groundwater flux. These results suggest that streams migrate, steepening the topography as they do.

5 Conclusion

We have presented evidence that stream migration can occur in response to an asymmetric groundwater table. We suggested that this migration is responsible for two planform features: a wide confluence angle and a network wide curvature fluctuation along the reach. First, we presented theoretical results that suggest that confluence migration according to this asymmetry would favor a symmetric configuration with a 120° angle near stream junctions, narrowing to a 72° angle near stream tips. We found evidence of such a feature in real streams. Second, we found that network-wide river curvature fluctuates at a length scale

comparable to the length scale of this deviation, and we presented topographic evidence that suggests that this fluctuation is a product of the same migration mechanism. Our results reveal the presence of a novel mechanism in Laplacian growth that may inform understanding of other thin-finger systems.

References

D.M. Abrams, A.E. Lobkovsky, A.P. Petroff, K.M. Straub, B. McElroy, D.C. Mohrig, A. Kudrolli, and D.H. Rothman. Growth laws for channel networks incised by groundwater flow. *Nature Geoscience*, 2(3):193–196, 2009.

J. Bear. *Dynamics of Fluids in Porous Media*. 1972.

J.L. Best. Sediment transport and bed morphology at river channel confluences. *Sedimentology*, 35(3):481–498, 1988.

P.R. Bierman and D.R. Montgomery. *Key Concepts in Geomorphology*. W.H. Freeman, 2013.

C.J. Carey, T.G. Brown, K.C. Challis, A.J. Howard, and L. Cooper. Predictive modelling of multiperiod geoarchaeological resources at a river confluence: a case study from the Trent–Soar, UK. *Archaeological Prospection*, 13(4):241–250, 2006.

L. Carleson and N. Makarov. Laplacian path models. *Journal d'Analyse Mathématique*, 87: 103–150, 2002.

Y. Cohen, O. Devauchelle, H.F. Seybold, R.S. Yi, P. Szymczak, and D.H. Rothman. Path selection in the growth of rivers. *Proceedings of the National Academy of Sciences*, 112 (46):14132–14137, 2015.

H. Darcy. *Les fontaines publiques de la ville de Dijon: exposition et application...* Victor Dalmont, 1856.

O. Devauchelle, A.P. Petroff, A.E. Lobkovsky, and D.H. Rothman. Longitudinal profile of channels cut by springs. *Journal of Fluid Mechanics*, 667:38–47, 2010.

O. Devauchelle, A.P. Petroff, H.F. Seybold, and D.H. Rothman. Ramification of stream networks. pages 2–6, 2012. doi: 10.1073/pnas.1215218109.

O. Devauchelle, P. Szymczak, M. Pecelerowicz, Y. Cohen, H.F. Seybold, and D.H. Rothman. Laplacian networks: Growth, local symmetry, and shape optimization. *Physical Review E*, 95(3):033113, 2017.

T. Dunne. Hydrology, mechanics, and geomorphic implications of erosion by subsurface flow. *Special Paper-Geological Society of America*, (252):1–28, 1990.

J. Dupuit. *Etudes theoriques et pratiques sur le mouvement des eaux dans les canaux decouverts et a travers les terrains permeables avec des considerations relatives au regime des grandes eaux, au debouche a leur donner et a la marche des alluvions dans les rivieres a fond mobile*. Dunod, 1863.

Robert I Ferguson. Meander irregularity and wavelength estimation. *Journal of Hydrology*, 26(3-4):315–333, 1975.

T. Gubiec and P. Szymczak. Fingered growth in channel geometry: A Loewner-equation approach. *Physical Review E*, 77, 2008.

R.R. Gutierrez, J.D. Abad, M. Choi, and H. Montoro. Characterization of confluences in free meandering rivers of the amazon basin. *Geomorphology*, 220:1–14, 2014.

E.J. Hickin and G.C. Nanson. Lateral migration rates of river bends. *Journal of Hydraulic Engineering*, 110(11):1557–1567, 1984.

J.M. Hooke. Changes in river meanders: a review of techniques and results of analyses. *Progress in Physical Geography*, 8(4):473–508, 1984.

R.E. Horton. Erosional development of streams and their drainage basins; hydrophysical approach to quantitative morphology. *Geological society of America bulletin*, 56(3):275–370, 1945.

A.D. Howard. Optimal angles of stream junction: Geometric, stability to capture, and minimum power criteria. *Water Resources Research*, 7(4):863–873, 1971a.

A.D. Howard. Simulation model of stream capture. *Geological Society of America Bulletin*, 82(5):1355–1376, 1971b.

A.D. Howard and C.F. McLane. Erosion of cohesionless sediment by groundwater seepage. *Water Resources Research*, 24(10):1659–1674, 1988.

B.A. Kennedy. On Playfair's law of accordant junctions. *Earth Surface Processes and Landforms*, 9(2):153–173, 1984.

W. Kühnel. *Differential geometry*, volume 77. American Mathematical Soc., 2015.

M. Marani, S. Lanzoni, D. Zandolin, G. Seminara, and A. Rinaldo. Tidal meanders. *Water Resources Research*, 38(11), 2002.

M.P. Mosley. An experimental study of channel confluences. *The journal of geology*, pages 535–562, 1976.

T.J. Nicoll and E.J. Hickin. Planform geometry and channel migration of confined meandering rivers on the canadian prairies. *Geomorphology*, 116(1):37–47, 2010.

A.P. Petroff, O. Devauchelle, D.M. Abrams, A.E. Lobkovsky, A. Kudrolli, and D.H. Rothman. Geometry of valley growth. *Journal of Fluid Mechanics*, 673:245–254, 2011.

A.P. Petroff, O. Devauchelle, H.F. Seybold, and D.H. Rothman. Bifurcation dynamics of natural drainage networks. *Philosophical Transactions of the Royal Society of London A: Mathematical, Physical and Engineering Sciences*, 371(2004):20120365, 2013.

P. Polubarinova-Kochina. Theory of ground water movement. *Princeton University Press*, 1962.

D.F. Ritter, R.C. Kochel, and J.R. Miller. *Process Geomorphology*. Waveland Press, Inc., 2011.

S.A. Schumm, K.F. Boyd, C.G. Wolff, and W.J. Spitz. A ground-water sapping landscape in the Florida panhandle. *Geomorphology*, 12(4):281–297, 1995.

H.F. Seybold, D.H. Rothman, and J.W. Kirchner. Climate's watermark in the geometry of stream networks. *Geophysical Research Letters*, pages n/a–n/a, 2017. ISSN 1944-8007. doi: 10.1002/2016GL072089. URL `http://dx.doi.org/10.1002/2016GL072089`. 2016GL072089.

J.G. Speight. Meander spectra of the Angabunga River. *Journal of Hydrology*, 3(1):1–15, 1965.

A.N. Strahler. Hypsometric (area-altitude) analysis of erosional topography. *Geological Society of America Bulletin*, 63(11):1117–1142, 1952.

M.G. Unde and S. Dhakal. Sediment characteristics at river confluences: a case study of the Mula-Kas confluence, Maharashtra, India. *Progress in Physical Geography*, 33(2):208–223, 2009.

E.W. Weisstein. Curvature. From MathWorld—A Wolfram Web Resource, 2017. URL `http://mathworld.wolfram.com/Curvature.html`. Last visited on 2017-06-21.

S.D. Willett, S.W. McCoy, J.T. Perron, L. Goren, and C.-Y. Chen. Dynamic reorganization of river basins. *Science*, 343(6175):1248765, 2014.

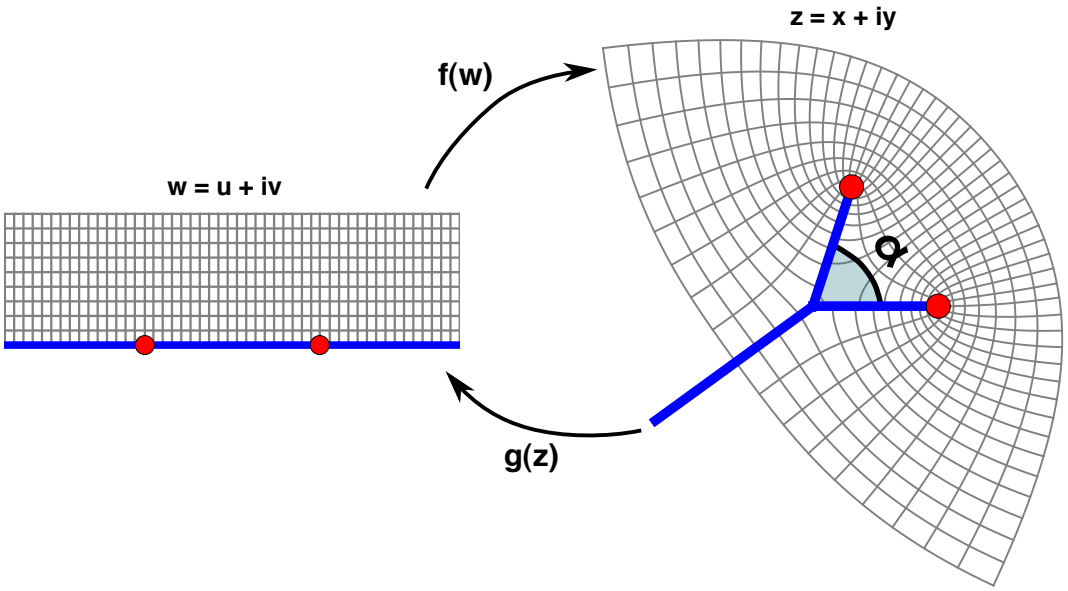

Figure 12: An illustration of the map from the upper half plane $w = u + iv$ to the physical plane $z = x + iy$ given by equation (12). The map has a single parameter $c = \alpha/2\pi$, where α is the angle between the two branches.

A Optimal migration angle

A.1 Conformal map

The general form of the conformal map which produces the fishtail shape in Figure 1 is

$$f(w) = w^{2c}\left(\frac{1}{c} - w^2\right)^{1-c}, \tag{12}$$

where c is the angle (α) between the two branches as a fraction of 2π. $f(w) : w \to z$ maps from the upper half plane, $w = u + iv$, to the physical plane $z = x + iy$. Because the Laplace equation 3 is conformally invariant, then the imaginary part of $f^{-1}(z) = g(z) : z \to w$ is harmonic and provides us with the shape of the groundwater field around the bifurcated geometry. This map is illustrated in Figure 12.

A.2 Flux

While we cannot invert $f(z)$ directly, we can calculate the flux jump implicitly in terms of the mathematical variable v by choosing a rotation of the map such that one of the branches lies along an axis. Conveniently, this is the case for (12), for which one branch lies along the positive x axis, as shown in Figure 12. The flux into this branch is therefore dv/dy, where v is the imaginary part of w. To this end, the derivative dz/dv is given by

$$\frac{\partial z}{\partial v} = 2ic\left(\frac{1}{c} - w^2\right)^{1-c} w^{2c-1} - 2i(1-c)\left(\frac{1}{c} - w^2\right)^{-c} w^{2c+1}. \tag{13}$$

And $\partial y/\partial v$ is the imaginary component of this quantity evaluated at $v = 0$:

$$\frac{\partial y}{\partial v} = -2Re\left(u^{2c-1}\left(\frac{1}{c} - u^2\right)^{-c}(u^2-1)\right). \tag{14}$$

If $0 < u \leq \frac{1}{\sqrt{c}}$, which is the range along the x-axis we are concerned with, the argument within Re is always real. The flux Q within this domain is given by the reciprocal of this quantity:

$$Q = \frac{\partial v}{\partial y} = -\frac{2}{u^{2c-1}\left(\frac{1}{c} - u^2\right)^{-c}(u^2-1)} \tag{15}$$

The flux jump is therefore implicitly defined by (12) and (15). An illustration of the resulting behavior for a few values of c is shown in figure 6(c).

A.3 Flux jump as $x \to 0$

Q exhibits a peculiar behavior: the flux Q and, consequently, the flux jump $[Q]$ go to 0 regardless of the choice of c. To demonstrate this analytically, we can calculate the limit of

(15) as $u \to 0, \frac{1}{\sqrt{c}}$, the roots that correspond to the junction. First, in the limit $u \to 0$,

$$\lim_{u\to 0} Q = \lim_{u\to 0} \frac{2}{u^{2c-1}c^c} \tag{16}$$

$$= 0, \tag{17}$$

assuming $c < 1/2$ (the bifurcation angle is less than π). Similarly, for $u \to \frac{1}{\sqrt{c}}$,

$$\lim_{u\to \frac{1}{\sqrt{c}}} Q = \lim_{u\to \frac{1}{\sqrt{c}}} \frac{-2\left(\frac{1}{c} - u^2\right)^c}{c^{\frac{2c-1}{2}}\left(\frac{1}{c} - 1\right)} \tag{18}$$

$$= 0, \tag{19}$$

assuming $c > 0$ (the bifurcation angle is greater than 0). The flux jump therefore also approaches 0 for all values of c as $x \to 0$.

A.4 Flux jump departs from 0 most slowly for $\alpha = 2\pi/3$

We seek to determine the rate at which flux jump departs 0 from the junction as a function of $c = \alpha/2\pi$. This can be found by solving $\frac{\partial^2 v}{\partial x \partial y} = 0$ for c. To this end, recall that ∂_z, the partial derivative with respect to z, and ∂_z^2 can be written in terms of x and y as

$$\partial_z = \frac{1}{2}\left(\partial_x - i\partial_y\right) \tag{20}$$

$$\partial_z^2 = \frac{1}{4}\left(\partial_x^2 - 2i\partial_x\partial_y + \partial_y^2\right). \tag{21}$$

The derivative $\frac{\partial^2 v}{\partial x \partial y}$ can therefore be rewritten in terms of z as

$$\frac{\partial^2 v}{\partial x \partial y} = -\frac{1}{2} Im\left(\frac{\partial^2 v}{\partial z^2}\right). \tag{22}$$

However, we only have $\partial v/\partial z$ in terms of u and v. We therefore require this expression to be rewritten in terms of $\partial^2 z/\partial^2 v$, which we can now calculate directly:

$$\frac{\partial^2 v}{\partial x \partial y} = -\frac{1}{2} Im\left(\frac{\partial^2 v}{\partial z^2}\right) \tag{23}$$

$$= \frac{1}{2} Im\left(\frac{\frac{\partial^2 z}{\partial v^2}}{\left(\frac{\partial z}{\partial v}\right)^3}\right). \tag{24}$$

We are only concerned with $w = u$, for $0 < u < \frac{1}{\sqrt{c}}$. Therefore,

$$\frac{\partial Q}{\partial x} = \frac{\partial^2 v}{\partial x \partial y} = \frac{1}{2} \frac{\left(\frac{1}{c} - u^2\right)^{2c} (a + b + c + d)}{\left(2c\left(\frac{1}{c} - u^2\right) u^{2c-1} - 2(1-c)u^{2c+1}\right)^3}, \tag{25}$$

where

$$a = 4(1-c)cu^{2c} \tag{26}$$

$$b = 2(1-c)(1+2c)u^{2c} \tag{27}$$

$$c = 2c(1-2c)\left(\frac{1}{c} - u^2\right) u^{2c-2} \tag{28}$$

$$d = 4(1-c)c\left(\frac{1}{c} - u^2\right)^{-1} u^{2+2c}. \tag{29}$$

We want $\partial_x[Q(x)] = \partial_x(Q(u_1(x)) + Q(u_2(x)))$ as a function of c as x approaches its roots. To this end, we invert the conformal map (12) in the limit as u approaches its roots, $u \to 0, \frac{1}{\sqrt{c}}$. Because we are dealing only with values on the real axis both in the mathematical and physical plane, we let $v = 0$ for equation (12). For small u, x is given by

$$x = f(u) = u^{2c}\left(\frac{1}{c} - u^2\right)^{1-c} \tag{30}$$

$$\approx u^{2c} c^{c-1}. \tag{31}$$

Similarly for $u \to 1/\sqrt{c}$,

$$x = f(u) = u^{2c}\left(\frac{1}{c} - u^2\right)^{1-c} \tag{32}$$

$$\approx c^{-c}\left(\frac{1}{c} - u^2\right)^{1-c}. \tag{33}$$

Inverting equations (31) and (33) gives us the two values of u that correspond to a single value of x,

$$u_1 = \left(\frac{x}{c^{c-1}}\right)^{\frac{1}{2c}},\ u_2 = \sqrt{\frac{1}{c} - x^{\frac{1}{1-c}}c^{\frac{c}{1-c}}}. \tag{34}$$

We combine equations (34) and (25) to obtain $\partial_x[Q(x)]$ explicitly for small x:

$$\partial_x[Q(x)] \approx \left.\frac{\partial Q}{\partial x}\right|_{u=\left(\frac{x}{c^{c-1}}\right)^{\frac{1}{2c}}} + \left.\frac{\partial Q}{\partial x}\right|_{u=\sqrt{\frac{1}{c}-x^{\frac{1}{1-c}}c^{\frac{c}{1-c}}}}. \tag{35}$$

Substituting these values in, we obtain an expression for $\partial_x[Q(x)]$ for small x:

$$\partial_x[Q(x)] \approx -\underbrace{\left(\frac{c^{\frac{1}{1-c}+\frac{1}{2}}}{4(c-1)^2}\right)}_{\alpha} x^{\frac{1}{1-c}-2} + \underbrace{\left(\frac{1}{8}c^{\frac{1}{2}\left(\frac{1}{c}-5\right)}(1-2c)\right)}_{\beta} x^{\frac{1}{2c}-2}. \tag{36}$$

To understand the behavior of this function, note that within the range $0 < c < 1/2$, both α and β are positive. Since we are concerned with the behavior of (36) in the vicinity of $c = 1/3$, we happily restrict ourselves to this range. For values on either side of $c = 1/3$, we have

$$\partial_x[Q(x)] \approx -\alpha x^{\frac{1}{1-c}-2} \to -\infty \text{ for } c < 1/3 \text{ as } x \to 0 \tag{37}$$

$$\partial_x[Q(x)] \approx \beta x^{\frac{1}{2c}-2} \to +\infty \text{ for } c > 1/3 \text{ as } x \to 0. \tag{38}$$

Therefore, $c = 1/3$ represents a special point for which the rate at which flux jump increases

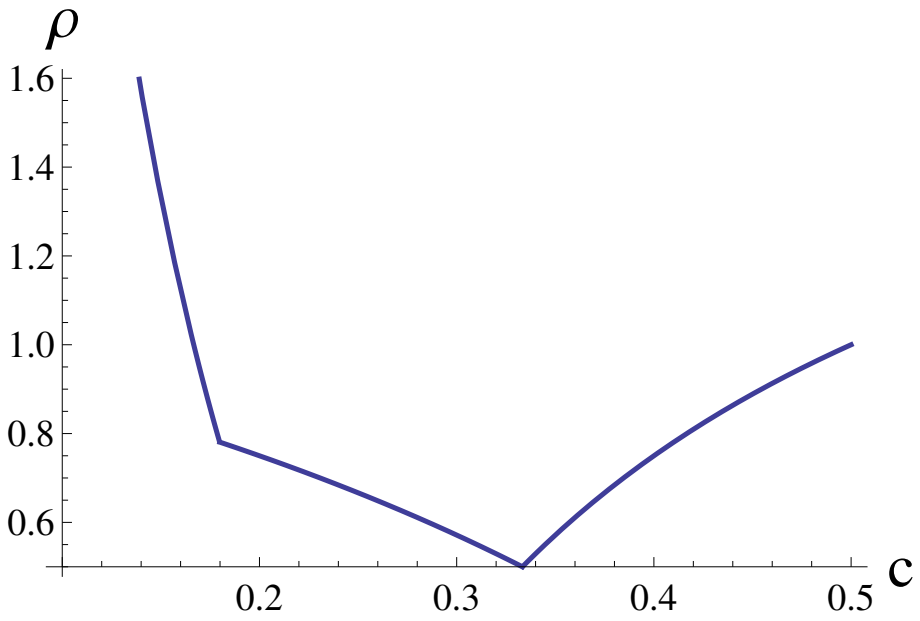

Figure 13: A plot of $\rho(c)$, as defined in equation (39).

with x near the junction is at a minimum. This can be seen by considering the quantity

$$\rho(c) = \max\left(\frac{1}{1-c} - 2,\ \frac{1}{2c} - 2\right) \tag{39}$$

where equation (38) for small x behaves as

$$\partial_x[Q(x)] \approx x^{\rho(c)}. \tag{40}$$

$\rho(c)$ is shown in figure 13, and as expected by our reasoning above, ρ has a minimum at $c = 1/3$, for which $\partial_x[Q[x]] \sim 1/\sqrt{x}$.